

Prospects for sub-nanometer scale imaging of optical phenomena using electron microscopy F

Cite as: Appl. Phys. Lett. **118**, 033104 (2021); <https://doi.org/10.1063/5.0029979>

Submitted: 18 September 2020 . Accepted: 07 December 2020 . Published Online: 21 January 2021

 Ze Zhang,  Archith Rayabharam,  Joel Martis, Hao-Kun Li,  Narayana R. Aluru, and  Arun Majumdar

COLLECTIONS

F This paper was selected as Featured



View Online



Export Citation



CrossMark



Your Qubits. Measured.

Meet the next generation of quantum analyzers

- Readout for up to 64 qubits
- Operation at up to 8.5 GHz, mixer-calibration-free
- Signal optimization with minimal latency

Find out more



Prospects for sub-nanometer scale imaging of optical phenomena using electron microscopy

Cite as: Appl. Phys. Lett. **118**, 033104 (2021); doi: [10.1063/5.0029979](https://doi.org/10.1063/5.0029979)

Submitted: 18 September 2020 · Accepted: 7 December 2020 ·

Published Online: 21 January 2021



View Online



Export Citation



CrossMark

Ze Zhang,¹  Archith Rayabharam,²  Joel Martis,¹  Hao-Kun Li,¹ Narayana R. Aluru,^{2,3} 
and Arun Majumdar^{1,4,5,a)} 

AFFILIATIONS

¹Department of Mechanical Engineering, Stanford University, Stanford, California 94305, USA

²Department of Mechanical Science and Engineering, University of Illinois at Urbana-Champaign, Urbana, Illinois 61801, USA

³Beckman Institute for Advanced Science and Technology, University of Illinois at Urbana-Champaign, Urbana, Illinois 61801, USA

⁴Department of Photon Science, SLAC National Accelerator Laboratory, Menlo Park, California 94025, USA

⁵Precourt Institute for Energy, Stanford University, Stanford, California 94305, USA

a) Author to whom correspondence should be addressed: amajumdar@stanford.edu

ABSTRACT

Imaging of optical phenomena at the sub-nanometer scale can offer fundamental insights into the electronic or vibrational states in atomic-scale defects, molecules, and nanoparticles, which are important in quantum information, heterogeneous catalysis, optoelectronics, and structural biology. Several techniques have surpassed the traditional Abbe diffraction limit and attained spatial resolutions down to a few nanometers, but sub-nanometer scale optics has remained elusive. Here, we propose an approach that combines spectrally specific photoabsorption with sub-nanometer scale resolution transmission electron microscopy (TEM) of photoexcited electrons. We first estimate the signal level and conditions required for imaging nanoscale optical phenomena in core-shell quantum dots (QDs) like CdS/CdTe. Furthermore, we show the possibility of imaging photoexcited states of atomic-scale defects in a monolayer hexagonal boron nitride (h-BN) using *ab initio* and high resolution (HR)TEM simulations. The ability to directly visualize photoexcited states at the sub-nanometer scale opens opportunities to study properties of individual quantum dots and atomic defects.

Published under license by AIP Publishing. <https://doi.org/10.1063/5.0029979>

Since the early 18th century, when Antonie van Leeuwenhoek made optical microscopes and showed single-cell organisms in rain water,¹ optical imaging has become a fundamental tool for numerous branches of science and engineering, with a continuous drive to observe light-induced phenomena at ever smaller scales. Optical phenomena contain rich information about the energy states of matter, which is important in fields such as quantum information, catalysis, optoelectronics, and structural biology.^{2–5} Many optical spectroscopy and imaging techniques like Raman, photoluminescence, and IR spectroscopy are widely used for materials characterization. However, their spatial resolutions are limited by the Abbe diffraction limit to the wavelength of light used, which is hundreds of nanometers to micrometers.^{6–9} Although various techniques like near-field or stochastic fluorescence super-resolution imaging,^{10,11} and scanning probe microscopy (SPM)^{12–14} have been developed to break this diffraction limit, their spatial resolutions are still limited and not adequate to optically image sub-nanometer scale features.¹⁵ In addition, fluorescence-based techniques need stable fluorescent labels, while near-field and scanning probe-based techniques have poor depth of field and are only

surface sensitive. Although certain scanning tunneling microscopy (STM)-based optical spectroscopy techniques have achieved sub-nanometer resolution, tip convolution and substrate-based effects have complicated data interpretation.¹⁶ A far-field transmission-based technique with sub-nanometer scale resolution will provide complementary capabilities to existing techniques and open more opportunities.

Modern aberration-corrected transmission electron microscopes (TEMs), on the other hand, can readily achieve sub-angstrom resolution using high-energy electrons (60–300 keV) with picometer wavelengths. However, the energy mismatch between such high-energy electrons and valence/vibrational electronic states (meV to a few eV) limits the chemical information that TEMs can provide.¹⁷ Only recently has it become possible to resolve sub-eV excitations in materials using electron energy loss spectroscopy (EELS).¹⁸ It has been used to probe isotope shifts, phonons, phonon-polaritons, and surface modes,^{19–24} but the sophisticated and costly instrumentation make the wide application challenging.

Here, we propose an imaging technique named PhotoAbsorption Microscopy using ELection Analysis (PAMELA), which combines

spectrally specific photoabsorption with atomic resolution transmission electron microscopy to obtain imaging of photoexcited states at nanometer and atomic scales. Figure 1 presents schematics of the PAMELA setup, where the sample is optically excited *in situ* during high-resolution TEM imaging through a custom-designed TEM holder containing an optical fiber. Atoms and molecules absorb ultraviolet (UV) or visible photons with their unique spectra based on the electronic states. Photoabsorption induces a redistribution of the local electron density corresponding to the wavefunction of the excited state in the optical absorbing regions, while other regions remain unaffected. The local charge density also changes the local potential distribution. When the high-energy electrons inside a TEM are transmitted through this modified charge and potential distribution, it changes phase and produces sub-nanometer-scale contrast in the final high resolution (HR) TEM image.

To detect such a small contrast change and eliminate the effects from sample drift and TEM instability, the laser intensity ΔI is modulated at a frequency $f_0 = f_V/4$, where f_V is the video framerate of the camera used in HRTEM. The HRTEM images are then processed to produce the DC ground state images (structural) and the AC difference images (optical). The DC ground state images are obtained by simple averaging, while the AC difference images are obtained by filtering the image via a frequency-domain image lock-in around f_0 with a bandwidth²⁵ $\Delta f \sim 1/T$, where T is the total averaging time. Note that $T \gg \tau$, where τ is the excited state lifetime. In the optically linear regime, the modulated electron density of the photoexcited state (ΔN_1) can be estimated by $\Delta N_1 = \alpha \Delta I \tau / h\nu$, where α is the absorption coefficient and $h\nu$ is the photon energy. With increasing ΔI , the number of photoexcited electrons will eventually reach

saturation, where half of them are in the excited state for a simple two-level system. With a lifetime $\tau \sim 1\text{--}10$ ns and a selected laser wavelength, saturation can be reached with relatively low optical flux. The detailed dependence about the percentage of electrons being excited with the laser intensity and the excited state lifetime is discussed in [supplementary material S8](#). In this paper, we discuss the possibility and experimental conditions for two model systems: (a) CdS/CdTe core-shell quantum dots (QDs); and (b) defects in hexagonal boron nitride (h-BN). In both cases, we use simulations and experimentally measured noise to estimate the signal-to-noise ratio (SNR) and offer the values of T that are needed to produce $\text{SNR} > 3$ (Rose criterion).²⁶

Photon-driven charge separation and charge transfer in nanomaterials like QDs play a critical role in photocatalytic and photovoltaic systems.^{27–29} Past attempts at uncovering charge transfer mechanisms have relied on transient optical spectroscopy measurements of an ensemble.³⁰ However, direct visualization of single particle photoexcited states has remained elusive. Here, we consider a CdS/CdTe core-shell QD with the dimensions shown in Fig. 2(a). When photoexcited by light of energy above the bandgap of CdTe, electron-hole pairs are created and the electrons are localized in the core, while the holes are localized in the shell due to the type II band alignment shown in Fig. 2(a). Using a simple potential well model, we calculate the first excited state of this quantum dot (details in [supplementary material S4](#)). The resulting probability distributions are plotted in Fig. 2(b), and as expected, we see that photoexcitation causes charge separation, with the electron (hole) being localized in the core (shell). This charge separation leads to a localized potential change [shaded area in Fig. 2(c)] and, hence, HRTEM contrast. An order of magnitude estimation of the HRTEM contrast C due to this potential change is³¹

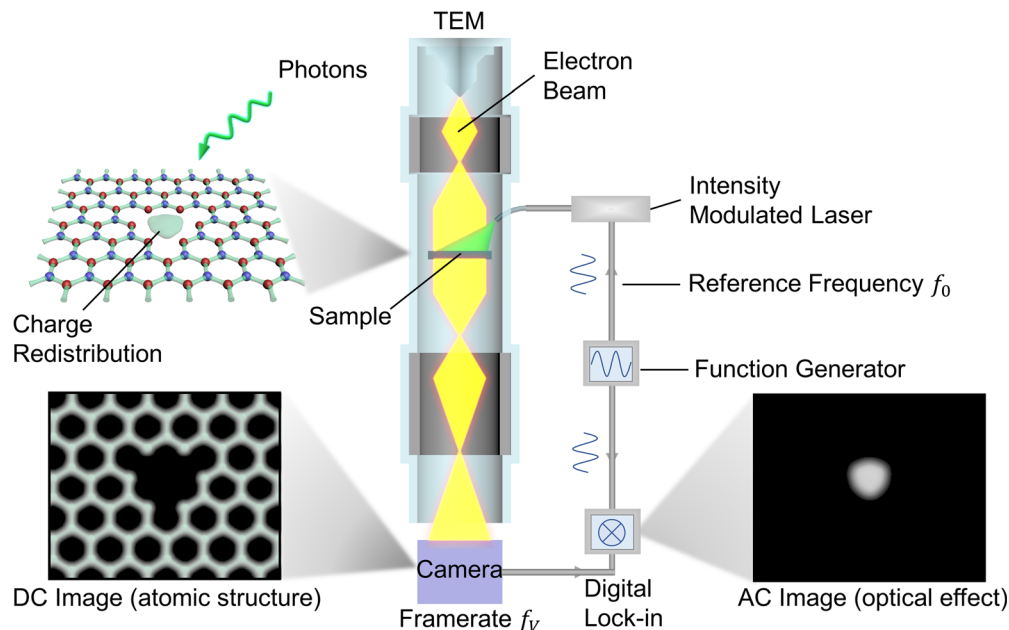


FIG. 1. Schematics of the PhotoAbsorption Microscopy using ELection Analysis (PAMELA-TEM) setup. An intensity modulated (at a frequency f_0) laser is introduced into a TEM to optically excite the sample (e.g., defects in h-BN). Photoexcitation of the defect leads to a localized charge redistribution, which is then imaged by the TEM camera with a framerate $f_V = 4f_0$. The HRTEM images are then processed using an image lock-in algorithm to produce the DC ground state image (structural information) and the AC difference image (optical information).

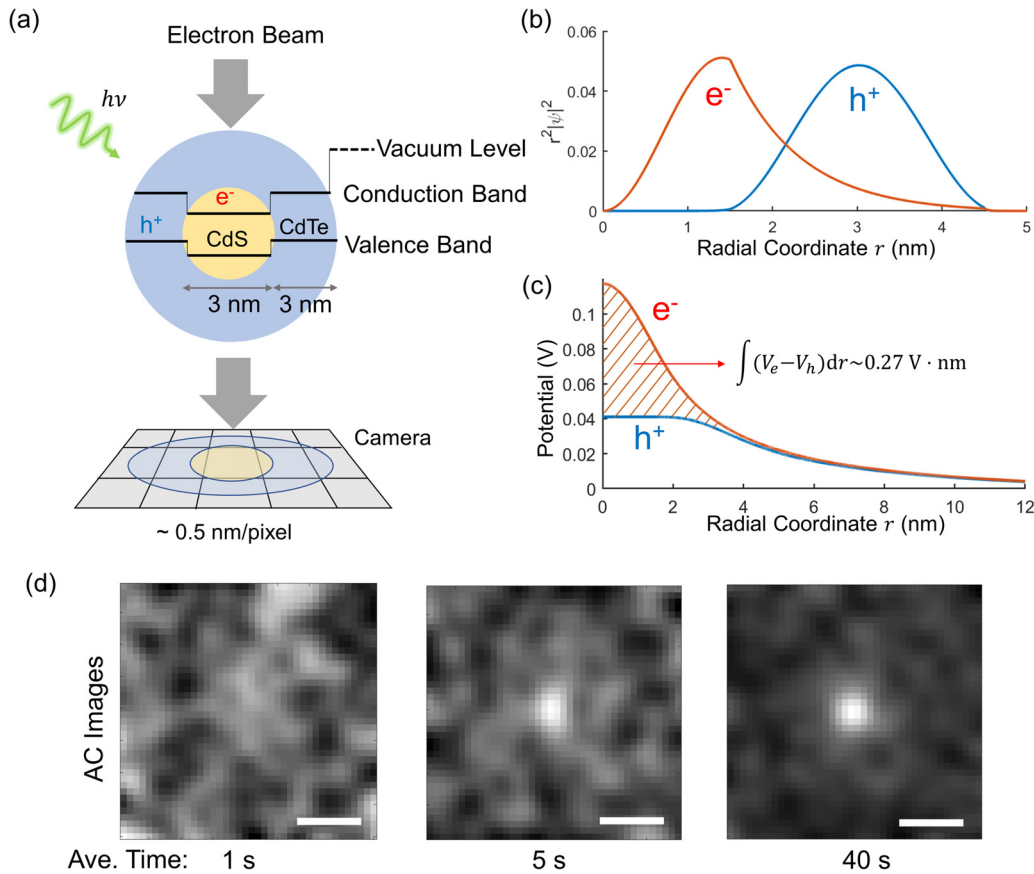


FIG. 2. Simulation of the photoexcited state in a CdS/CdTe core/shell quantum dot. (a) Schematic of a CdS/CdTe core-shell quantum dot detailing the band alignment and imaging setup. (b) Electron/hole wavefunctions for the first excited state as a function of the radial coordinate. The shaded area represents the potential difference due to electron-hole separation. (c) Phase contrast images (Gaussian filtered with a standard deviation of 0.8 nm) of the photoexcited state with shot noise, estimated using the 2D projected potential of the photoexcited state using a defocus of $-1 \mu\text{m}$ and aberration coefficient C_s of 1 nm. Scale bars are 5 nm.

$$C = \frac{\pi \int V dz}{\lambda E_0} = \frac{\pi * 0.27 \text{ V} \cdot \text{nm}}{4.8 \text{ pm} * 60 \text{ keV}} = 0.00294, \quad (1)$$

where V is the photoinduced potential, z is the coordinate along the primary beam direction, λ is the primary electron wavelength, and E_0 is the primary electron beam energy. The imaging time T required for an SNR of 3 is calculated assuming a dose rate of $10^4 \text{ e}^-/\text{\AA}^2/\text{s}$ and a pixel size of 0.5 nm (corresponding to a dose rate $D \sim 2.5 \times 10^5 \text{ e}^-/\text{pixel}$):

$$T \sim \left(\frac{\text{SNR}}{C * \sqrt{D}} \right)^2 = \left(\frac{3}{0.00294 * \sqrt{2.5 \times 10^5}} \right)^2 = 5 \text{ (s)}. \quad (2)$$

Figure 2(d) shows phase contrast images with shot noise for different averaging times. Since $T = 5 \text{ s}$ of averaging time in HRTEM is quite feasible and core-shell QDs are robust under electron beam irradiation, these core-shell QDs can be a promising material system to perform proof-of-concept experiments for demonstrating the PAMELA-TEM technique.

Second, to explore atomic-scale resolution, we consider defects in h-BN, which have recently been shown to be room-temperature single

photon emitters (SPEs)³² with potential applications in quantum information. Despite wide interest, the origin of these SPEs is still under debate. Several studies have attempted to infer the correlation between the atomic-scale defect structures and optical properties using simulations or correlative imaging.^{33–36} Here, we show that PAMELA-TEM provides a direct way to image photoexcited states of defects in h-BN, thus establishing a conclusive correlation between the atomic structure and optical properties.

We first use self-consistent density functional theory (DFT) simulations to calculate the band structure [Fig. 3(b)] and the electron distribution for an anti-site nitrogen vacancy $N_B V_N$ defect in a monolayer h-BN [Fig. 3(a)]. Pristine h-BN has a wide bandgap, while defects introduce in-gap states. This $N_B V_N$ defect is proposed to be a single photon emitter.³² Figure 3(c) shows the projected ground-state electron charge distribution. The defect-induced in-gap states can be optically excited by choosing specific laser wavelengths. Upon photoexcitation, some electrons are excited to higher energy states, and this causes charge redistribution. For SPEs in h-BN, their lifetime is usually nanoseconds and saturation is reached with relatively low optical flux.³² So here we assume that the excited state is fully saturated with a

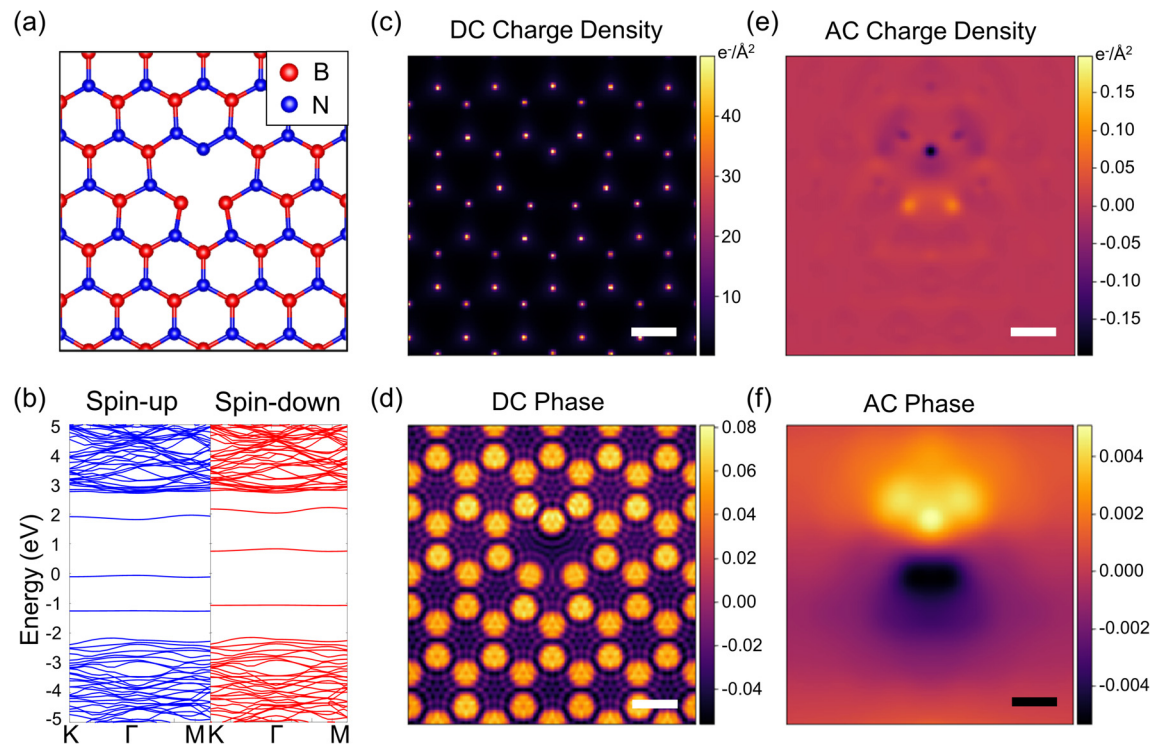


FIG. 3. Simulation results of an anti-site nitrogen vacancy $N_B V_N$ defect in a monolayer h-BN. (a) Atomic structure and (b) spin-polarized band structure of the defect. (c) Ground state projected charge density distribution. (d) Phase change of the exit electron beam after going through the sample at the ground state. (e) Charge redistribution due to photoexcitation. (f) The difference of phase change between the photoexcited state and the ground state. The electron phase change is simulated using 60 keV incident electron beam energy. Scale bars are 2 Å.

continuous wave laser excitation. The difference in the charge distribution between the ground and the first excited state is shown in Fig. 3(e). We then include the charge from the nucleus, solve three-dimensional Poisson's equation for the electrical potential of the sample, and perform multislice simulations^{37,38} with 60 keV incident electron beams. Figure 3(d) shows the electron phase map for the ground state potential and Fig. 3(f) is the difference in the phase map due to charge redistribution. The electron phase difference between the ground state and the excited state preserves the atomic scale feature from the charge density distribution.

HRTEM images of the same object can vary significantly based on the defocus and the aberration of the magnetic lens used for imaging.³¹ To understand the effect of lens defocus and spherical aberration values (C_s) on HRTEM images, different contrast transfer functions are implemented and the matrix of ground-state images is shown in Fig. 3(a). The difference image matrix between the photoexcited and ground states is shown in Fig. 3(b). It is clear that there is a compromise between contrast and spatial resolution—while a smaller defocus produces sharper features, it is inevitably accompanied by a decrease in contrast. Also, it is seen that while an uncorrected microscope ($C_s \sim 1$ mm) can resolve the pristine lattice, spherical aberration correction (C_s less than tens of μm) is needed to resolve the detailed defect structure. The actual HRTEM images captured by the camera need to consider various sources of noise, such as shot noise of electrons and camera noise. We choose a defocus of 20 nm and a spherical

aberration coefficient of $C_s = -50 \mu\text{m}$ [red circled images in Figs. 4(a) and 4(b)] and add shot noise and camera noise to the calculation. The camera read noise is found to be insignificant relative to the shot noise for a K3 direct electron camera (see supplementary material S5). Images with electron doses from 5×10^4 to $1.2 \times 10^6 \text{ e}^-/\text{\AA}^2$ are shown in Fig. 4(c). The pixel sizes are 0.2 \AA for the ground-state images and the difference images. A Gaussian filter with a 0.7 \AA standard deviation is used to remove the high-frequency noise in the difference images and does not affect the resulting optical contrast (which extends to $> 3 \text{ \AA}$).³⁹ Assuming a dose rate of $10^4 \text{ e}^-/\text{\AA}^2/\text{s}$, acquisition times in Fig. 4(c) vary from 5 to 120 s for the doses listed above. We see that after about 40 s of averaging, the optical signature of the excited state starts to be visible, while 120 s of averaging makes the difference image much clearer. This suggests that atomic-scale imaging with optical information using PAMELA-TEM is achievable. We further calculate the SNR values for different accumulated doses as shown in Fig. 4(d), where the signal is obtained from averaging the intensity within 0.5 \AA of the defects and then subtracting the background, while the noise is the standard deviation of the background. The shaded area represents uncertainty of one standard deviation for ten independent simulations. The SNR increases with the square root of the dose, which provides guidance for the imaging condition one should use for experiments.

The feasibility of atomic scale PAMELA-TEM imaging also depends on the stability of the instrumentation and the sample. Thanks to the constant development of TEM instrumentations, the

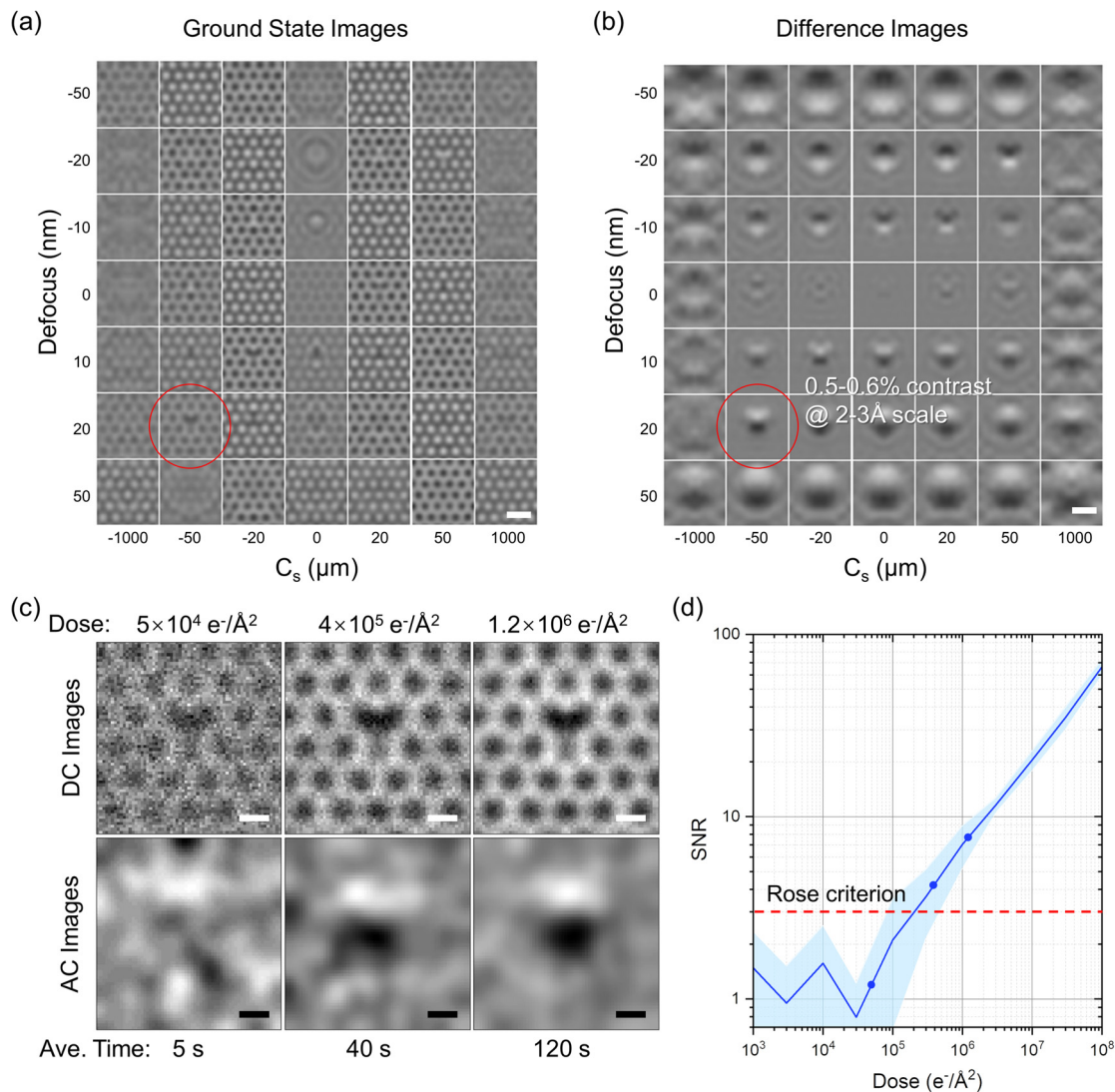


FIG. 4. TEM simulations of an anti-site nitrogen vacancy $N_B V_N$ defect in a monolayer h-BN. (a) Structural images (DC images) under different defocus and aberration coefficients. (b) Optical images (AC images) obtained by calculating the difference between the excited and ground state images. The red circled images show the condition we use for simulations with noise in (c). (c) The top row images are for the ground state (0.2 Å/pixel sampling rate) and the bottom row images are the difference between the excited and the ground state images (Gaussian filtered with a standard deviation of 0.7 Å). Different columns show different doses (5×10^4 – 1.2×10^6 $e^-/\text{Å}^2$) and corresponding acquisition time (5–120 s) required. (d) Signal-to-noise ratio (SNR) with different doses. The shaded area represents the uncertainty of one standard deviation for ten independent simulations. Three dots indicate the conditions used in (c). The incident electron beam energy is 60 keV. Scale bars are 5 Å in (a) and (b) and 2 Å in (c).

required stability of the sample holders and microscope conditions are not out of reach. For example, the Transmission Electron Aberration-corrected Microscope (TEAM I) developed at the National Center for Electron Microscopy (NCEM) has demonstrated ultralow drift (~ 11 pm/min) and ultra-stable microscope parameters over tens of minutes and even hours.⁴⁰ Post processing algorithms for drift correction and image registration will further help the long acquisition times. Another key challenge is the high dose needed to observe a small photoinduced contrast change. Meyer *et al.*³⁹ experimentally measured the charge redistribution due to chemical bonding in monolayer graphene and h-BN, where they measured 0.5% signal with 0.08% standard

deviation using > 30 exposures.³⁹ This signal and noise level are comparable with what is required for the PAMELA-TEM measurements. In addition, tomography and EELS have reached atomic scale resolution recently,^{21,22,41} which require a similar or sometimes even higher dose than what we suggest here.

Since photoexcitation-driven charge redistribution is relatively small (< 1 $e^-/\text{Å}^2$), it requires a large dose ($\sim 10^5$ $e^-/\text{Å}^2$) to produce sufficient contrast for imaging. The ultimate spatial resolution of PAMELA-TEM, therefore, depends on the maximum dose a material can withstand before degrading under the electron beam. Degradation typically occurs via (i) displacement damage (knock-on or sputtering

events), where a primary electron undergoing elastic scattering with the nucleus transfers sufficient energy to dislodge the nucleus; or (ii) ionization damage (radiolysis), where a primary electron undergoes inelastic scattering and produces secondary electrons within the material that degrade chemical bonds.^{42,43} Knock-on damage typically occurs only above a certain threshold voltage. Pristine h-BN has been found to have a knock-on threshold of approximately 80 keV for boron and 120 keV for nitrogen. Defects, however, are more susceptible and have lower damage thresholds of around 40–60 keV.^{44,45} This suggests that a low voltage HRTEM (such as with the 20 keV SALVE III)⁴⁶ might be ideal for imaging photoexcited states. Low voltage imaging has the additional benefit of increased contrast per electron (Fig. S8). Since radiolysis increases with decreasing voltage, one might expect an optimum voltage with a compromise between knock-on damage and radiolysis. However, the ratio of contrast to inelastic scattering cross section is almost independent of incident electron energy for typical electron beam energies.⁴³ While liquid nitrogen specimen cooling has been found to help,^{43,47} other possibilities such as averaging over many particles or defects could be useful. Averaging is routinely used in cryo-EM where samples are highly dose sensitive ($<100 \text{ e}^-/\text{\AA}^2$),^{48,49} which then raises the possibility of PAMELA being combined with cryo-EM to chemically image biomolecules and proteins. One example is tris(bipyridine)ruthenium(II) ($\text{Ru}(\text{bpy})_3^{2+}$), which is a transition metal complex widely used in optical chemical sensing. We include the simulation results and dose requirements in the [supplementary material](#) (S10).

In summary, we have proposed an imaging technique named PAMELA-TEM, which combines optical excitation and electron microscopy to achieve sub-nanometer scale imaging of optical phenomena. The feasibility has been discussed for core-shell CdS/CdSe QDs and atomic scale defects in h-BN using DFT and HRTEM simulations. As PAMELA relies on the inherent light absorption and electron charge redistribution, it could be a general approach probing optical phenomena in materials with sub-nanometer scale spatial resolution. A continuous tunable wavelength light source will offer even better spectral information in the future. Furthermore, it could be interesting to study the effect of direct and indirect absorption. With atomic-scale resolution, we can potentially directly observe the lattice distortion during the indirect absorption process and further study the coupling between photons, phonons, electrons, and holes inside the sample. This sub-nanometer scale imaging of optical phenomena could open opportunities in multiple fields including defect engineering, heterogeneous catalysis, biosensing, and imaging.

See the [supplementary material](#) for details about DFT simulations, HRTEM simulations, experimental characterization of TEM camera noise, simulation results of other types of defects, organic molecules, effects of beam acceleration voltages, excited state lifetime, and corresponding supplementary figures.

AUTHORS' CONTRIBUTIONS

Z.Z. and A.R. contributed equally to this work.

The authors would like to thank Charles Martin (U. Florida); John Fourkas, YuHuang Wang, and John Cumings (U. Maryland); Tuan Ahn Pham and Eric Schwegler (Lawrence Livermore National Laboratory); Michael Strano (MIT); and Paul Alivisatos and

Andrew Minor (UC Berkeley) for their scientific insights and suggestions. This work was supported as part of the Center for Enhanced Nanofluidic Transport (CENT), an Energy Frontier Research Center funded by the U.S. Department of Energy, Office of Science, Basic Energy Sciences under Award No. DE-SC0019112. Z.Z. and J.M. acknowledge financial support from the Air Force Office of Scientific Research under Grant No. FA9550-19-1-0309. The *ab initio* simulations (DFT and GW) were carried out on the Blue Waters, supported by the National Science Foundation (Award Nos. OCI-0725070 and ACI-1238993) the State of Illinois, and as of December, 2019, the National Geospatial-Intelligence Agency. Blue Waters is a joint effort of the University of Illinois at Urbana-Champaign and its National Center for Supercomputing Applications. Part of the work was performed at the Stanford Nano Shared Facilities (SNSF), supported by the National Science Foundation under Award No. ECCS-1542152. K3 IS camera and support are courtesy of Gatan.

DATA AVAILABILITY

The data that support the findings of this study are available from the corresponding author upon reasonable request.

REFERENCES

- 1A. van Leeuwenhoek, *Ontledingen en Ontdekkingen Van Levende Dierkens in de Teel-Deelen Van Verscheyde Dieren, Vogelen en Visschen; Van Het Hout Met Der Selver Menigvuldige Vaaten; Van Hair, Vlees en Vis; Als Mede Van de Grootte Menigte Der Dierkens in de Excrementen*. (Boekverkooper, op't Rapenburg, London, 1702).
- 2I. Aharonovich, D. Englund, and M. Toth, *Nat. Photonics* **10**(10), 631 (2016).
- 3J. Hong, C. Jin, J. Yuan, and Z. Zhang, *Adv. Mater.* **29**(14), 1606434 (2017).
- 4W. Hou and S. B. Cronin, *Adv. Funct. Mater.* **23**(13), 1612 (2013).
- 5V. Ntziachristos, *Nat. Methods* **7**(8), 603 (2010).
- 6N. Colthup, *Introduction to Infrared and Raman Spectroscopy* (Elsevier, 2012).
- 7J. W. Lichtman and J.-A. Conchello, *Nat. Methods* **2**(12), 910 (2005).
- 8R. L. McCreey, *Raman Spectroscopy for Chemical Analysis* (John Wiley & Sons, 2005).
- 9H. W. Siesler, Y. Ozaki, S. Kawata, and H. M. Heise, *Near-Infrared Spectroscopy: Principles, Instruments, Applications* (John Wiley & Sons, 2008).
- 10E. Betzig, G. H. Patterson, R. Sougrat, O. W. Lindwasser, S. Olenych, J. S. Bonifacio, M. W. Davidson, J. Lippincott-Schwartz, and H. F. Hess, *Science* **313**(5793), 1642 (2006).
- 11A. Harootunian, E. Betzig, M. Isaacson, and A. Lewis, *Appl. Phys. Lett.* **49**(11), 674 (1986).
- 12F. Zenhausern, M. P. O'Boyle, and H. K. Wickramasinghe, *Appl. Phys. Lett.* **65**(13), 1623 (1994).
- 13R. M. Stöckle, Y. D. Suh, V. Deckert, and R. Zenobi, *Chem. Phys. Lett.* **318**(1–3), 131 (2000).
- 14F. Zenhausern, Y. Martin, and H. K. Wickramasinghe, *Science* **269**(5227), 1083 (1995).
- 15C. G. Galbraith and J. A. Galbraith, *J. Cell Sci.* **124**(10), 1607 (2011).
- 16A. Wallum, H. A. Nguyen, and M. Gruebele, *Annu. Rev. Phys. Chem.* **71**(1), 415 (2020).
- 17R. F. Egerton, *Electron Energy-Loss Spectroscopy in the Electron Microscope* (Springer Science & Business Media, 2011).
- 18O. L. Krivanek, T. C. Lovejoy, N. Dellby, T. Aoki, R. W. Carpenter, P. Rez, E. Soignard, J. Zhu, P. E. Batson, M. J. Lagos, R. F. Egerton, and P. A. Crozier, *Nature* **514**(7521), 209 (2014).
- 19P. Rez, T. Aoki, K. March, D. Gur, O. L. Krivanek, N. Dellby, T. C. Lovejoy, S. G. Wolf, and H. Cohen, *Nat. Commun.* **7**(1), 10945 (2016).
- 20M. J. Lagos, A. Trügler, U. Hohenester, and P. E. Batson, *Nature* **543**(7646), 529 (2017).

- ²¹J. A. Hachtel, J. Huang, I. Popovs, S. Jansone-Popova, J. K. Keum, J. Jakowski, T. C. Lovejoy, N. Dellby, O. L. Krivanek, and J. C. Idrobo, *Science* **363**(6426), 525 (2019).
- ²²K. Venkatraman, B. D. A. Levin, K. March, P. Rez, and P. A. Crozier, *Nat. Phys.* **15**(12), 1237 (2019).
- ²³R. Senga, K. Suenaga, P. Barone, S. Morishita, F. Mauri, and T. Pichler, *Nature* **573**(7773), 247 (2019).
- ²⁴F. S. Hage, G. Radtke, Z. M. Wang, M. Kepaptsoglou, M. Lazzeri, and Q. M. Ramasse, *Science* **367**(6482), 1124 (2020).
- ²⁵S. Grauby, B. C. Forget, S. Holé, and D. Fournier, *Rev. Sci. Instrum.* **70**(9), 3603 (1999).
- ²⁶A. Rose, *Adv. Electron. Electron Phys.* **1**, 131 (1948).
- ²⁷K. V. Vokhmintsev, P. S. Samokhvalov, and I. Nabiev, *Nano Today* **11**(2), 189 (2016).
- ²⁸K. Wu and T. Lian, *Chem. Soc. Rev.* **45**(14), 3781 (2016).
- ²⁹G. S. Selopal, H. Zhao, Z. M. Wang, and F. Rosei, *Adv. Funct. Mater.* **30**(13), 2070086 (2020).
- ³⁰L. Amirav and A. P. Alivisatos, *J. Am. Chem. Soc.* **135**(35), 13049 (2013).
- ³¹C. B. Carter and D. B. Williams, *Transmission Electron Microscopy: Diffraction, Imaging, and Spectrometry* (Springer, 2016).
- ³²T. T. Tran, K. Bray, M. J. Ford, M. Toth, and I. Aharonovich, *Nat. Nanotechnol.* **11**(1), 37 (2016).
- ³³J. Feng, H. Deschout, S. Caneva, S. Hofmann, I. Lončarić, P. Lazić, and A. Radenovic, *Nano Lett.* **18**(3), 1739 (2018).
- ³⁴F. Hayee, L. Yu, J. L. Zhang, C. J. Ciccarino, M. Nguyen, A. F. Marshall, I. Aharonovich, J. Vučković, P. Narang, T. F. Heinz, and J. A. Dionne, *Nat. Mater.* **19**(5), 534 (2020).
- ³⁵P. Dev, *Phys. Rev. Res.* **2**(2), 022050 (2020).
- ³⁶D. Kozawa, A. G. Rajan, S. X. Li, T. Ichihara, V. B. Koman, Y. Zeng, M. Kuehne, S. K. Iyemperumal, K. S. Siltmore, and D. Parviz, preprint [arXiv:1909.11738](https://arxiv.org/abs/1909.11738) (2019).
- ³⁷E. J. Kirkland, *Advanced Computing in Electron Microscopy* (Springer, 1998).
- ³⁸J. Madsen, see <https://github.com/jacobjma/PyQSTEM> for “PyQSTEM (2017)”
- ³⁹J. C. Meyer, S. Kurasch, H. J. Park, V. Skakalova, D. Künzel, A. Groß, A. Chuvilin, G. Algara-Siller, S. Roth, T. Iwasaki, U. Starke, J. H. Smet, and U. Kaiser, *Nat. Mater.* **10**(3), 209 (2011).
- ⁴⁰P. Ercius, M. Boese, T. Duden, and U. Dahmen, *Microsc. Microanal.* **18**(4), 676 (2012).
- ⁴¹Y. Yang, C.-C. Chen, M. C. Scott, C. Ophus, R. Xu, A. Pryor, L. Wu, F. Sun, W. Theis, J. Zhou, M. Eisenbach, P. R. C. Kent, R. F. Sabirianov, H. Zeng, P. Ercius, and J. Miao, *Nature* **542**(7639), 75 (2017).
- ⁴²R. F. Egerton, P. Li, and M. Malac, *Micron* **35**(6), 399 (2004).
- ⁴³R. F. Egerton, *Ultramicroscopy* **127**, 100 (2013).
- ⁴⁴J. Kotakoski, C. H. Jin, O. Lehtinen, K. Suenaga, and A. V. Krashennnikov, *Phys. Rev. B* **82**(11), 113404 (2010).
- ⁴⁵J. C. Meyer, A. Chuvilin, G. Algara-Siller, J. Biskupek, and U. Kaiser, *Nano Lett.* **9**(7), 2683 (2009).
- ⁴⁶M. Linck, P. Hartel, S. Uhlemann, F. Kahl, H. Müller, J. Zach, M. Haider, M. Niestadt, M. Bischoff, J. Biskupek, Z. Lee, T. Lehnert, F. Börrnert, H. Rose, and U. Kaiser, *Phys. Rev. Lett.* **117**(7), 076101 (2016).
- ⁴⁷E. Knapek and J. Dubochet, *J. Mol. Biol.* **141**(2), 147 (1980).
- ⁴⁸J. Frank, A. Verschoor, and M. Boublik, *Science* **214**(4527), 1353 (1981).
- ⁴⁹E. Nogales and S. H. Scheres, *Mol. Cell* **58**(4), 677 (2015).